Journal of Micromechatronics, Vol. 3, No. 2, pp. 75–101 (2006)

Also available online - www.vsppub.com

Controlled rolling of microobjects for autonomous manipulation

D. SINAN HALIYO *, FABIEN DIONNET and STÉPHANE REGNIER

Laboratoire de Robotique de Paris, Univ. Paris 6 CNRS, BP 61, 92265 Fontenay aux Roses, France

Abstract—This paper presents our work in developing an autonomous micromanipulation system. The originality of our system is that it takes advantage of adhesion forces to grip micro-objects using an AFM (Atomic Force Microscopy) probe. A theoretical analysis of rolling conditions is carried out in order to achieve precise release of an object picked-up by adhesion. Vision control, based on the specificities of optical microscopy, and force control, based on the analysis of the AFM probe, are established. Experiments validate the employed techniques and the proposed manipulation mode.

Keywords: Micromanipulation; microphysics; adhesion forces; rolling; sliding; force control; vision control.

1. INTRODUCTION

Due to recent development of MEMS and biotechnology, there is a great demand for original micromanipulation techniques. Many approaches have been proposed to manipulate microscopic objects. The principal obstacle specific to this scale is that the force of gravity becomes negligible in comparison with adhesion forces [1]. Consequently, any microsystem based on the miniaturisation of conventional macroscopic robots encounters a lot of difficulties in releasing a gripped object as it adheres to the gripper [2, 3]. Complex techniques, such as electrostatic detachment, are, thus, necessary to reduce adhesion [4].

Whatever the employed technique (with contact or not) and the environment (in air, liquid or vacuum) [5], due to specific mechanical and physical laws which govern the micro-world, micromanipulation systems often suffer from a lack of reproducibility. This is why micromanipulation tasks need complex and robust control based on sensor feedback.

*To whom correspondence should be addressed. E-mail: haliyo@robot.jussieu.fr

An original approach has been developed at Laboratoire de Robotique de Paris (LRP) which consists of taking advantage of adhesion to manipulate objects with a single fingered gripper. We showed that pick-up under quasi-static conditions is possible by choosing the material of the substrate on which the object is lying, so that adhesion between object and gripper is greater than between object and substrate [6]. We have also described a way to dynamically release an object [7]. The gripper is excited to induce high object accelerations. Contact is broken if the inertial force is greater than the adhesion force. This system is not only an operational micromanipulation station, but also a measurement platform, as explained in Ref. [8].

An alternative release mode is described in this paper. First, a theoretical analysis of microobject rolling is first presented. The goal is to find out conditions for contact force and gripper motion allowing to roll the object. This analysis shows the need for robust control for contact force and positioning. The implementation of such control schemes is described next, in particular focusing and image-based visual servoing, used to position the gripper accurately close to the object to be gripped. The force sensing capabilities are described in detail and results of impact and contact force control are discussed. Finally, first experiments of release by rolling and potential applications for micro-mechanical characterisations are presented.

2. THEORETICAL ANALYSIS

Adhesion phenomena are mainly the result of intermolecular potentials, as expressed by Van der Waals forces [9]. Capillarity and electrostatic are also environment-dependent forces that contribute to the adhesion. A theoretical study of these forces is presented in our earlier works [10].

For micro-scale objects, these forces have higher magnitudes than the gravitational force and they are mainly attractive. Nevertheless, they depend on the inverse square or cube of the distance between the surfaces, for example, for Van der Waals forces, and their influence becomes obvious in contact. A minimum amount of force is, thus, necessary to separate two media in contact. This force is commonly called 'pull-off'. In case of a sphere (radius R) on planar surface, its expresion is approximately given by Johnson–Kendall–Roberts (JKR, for the lower boundary) or Derjaguin–Muller–Toporov (DMT, for the higher boundary) contact models [11, 12].

$$\frac{3}{2}\pi R W_{ij} \leqslant F_{\text{pull-off}} \leqslant 2\pi R W_{ij}, \tag{1}$$

where W_{ij} is the Van der Waals potential between the two media i and j.

Under these circumstances, it is clear that classical multi-finger gripper architecture is not well adapted for micromanipulation, unless the adhesion could be considerably reduced, as the gripped objects stick to the gripper and the release is often hazardous. The reduction of adhesion can be achieved by choosing materials with

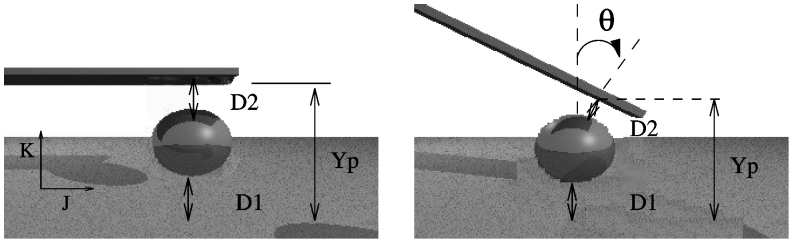

Figure 1. Description of the micro-manipulation task.

weak Van der Waals potentials or by the use of rough surfaces, but in most cases it is not possible to guarantee a macroscale-like behaviour.

However, it is possible to take advantage of the adhesion for gripping, with the use of high surface energy and a low surface roughness tool. In this case, one can pick up a micro-object by simple contact (Fig. 1). This approach is very interesting as it does not need a complex gripper architecture for grasping. The obvious problem in this case is the release, as it is necessary to overcome the adhesion between the gripping tool and the object. The use of the inertial force is a possible solution. To study its feasability, the dynamical analysis of the release task, including contact and adhesion forces, is performed. The established model, considering only vertical motion, is as follows:

$$m_{\mathrm{t}}\ddot{Y}_{\mathrm{p}} = F^{\mathrm{t}}_{\mathrm{ext}} - F^{\mathrm{ot}}_{\mathrm{adh}}(D_2) - m_{\mathrm{t}}g, \tag{2}$$

$$m_{\mathrm{o}}\ddot{D}_1 = F^{\mathrm{ot}}_{\mathrm{adh}}(D_2)\cdot\cos\theta - F^{\mathrm{os}}_{\mathrm{adh}}(D_1) - m_{\mathrm{o}}g, \tag{3}$$

$$Y_{\mathrm{p}} = D_1 + 2R_{\mathrm{o}} + D_2\cdot\cos\theta; \quad \ddot{D}_2\cdot\cos\theta = \ddot{Y}_{\mathrm{p}} - \ddot{D}_1, \tag{4}$$

where $m_{\mathrm{t}}, m_{\mathrm{o}}$ are, respectively, the mass of the gripping tool and the object, $F^{\mathrm{t}}_{\mathrm{ext}}$ is the external force applied to the gripper, and $F^{\mathrm{ot}}_{\mathrm{adh}}$ and $F^{\mathrm{os}}_{\mathrm{adh}}$ are, respectively, the adhesion forces between the object and the gripper and the object and the substrate, including Van der Waals, electrostatic and capillary forces. These forces are non-linear functions of distances $D_{1,2}$. R_{o} is the radius of the object, which is supposed to be a perfect sphere.

Simulations of the dynamic model show the existence of a value of initial acceleration $\ddot{Y}_{\mathrm{p}}$ of the gripper over which inertial effects overbalance the adhesion between the tool and the object, causing the release. This acceleration depends on both the mass of the object and the angle of slope θ of the gripper, as illustrated in Fig. 2 for a glass object of radius R initially adhering to a planar silicon gripper.

A close examination of these simulation results leads to the conclusion that, in order to achieve the release accurately, accelerations ranging from 10^4 to 10^6 m/s^2 are needed. A more detailed description of this dynamic release mode has been presented in one of our earlier publications [7].

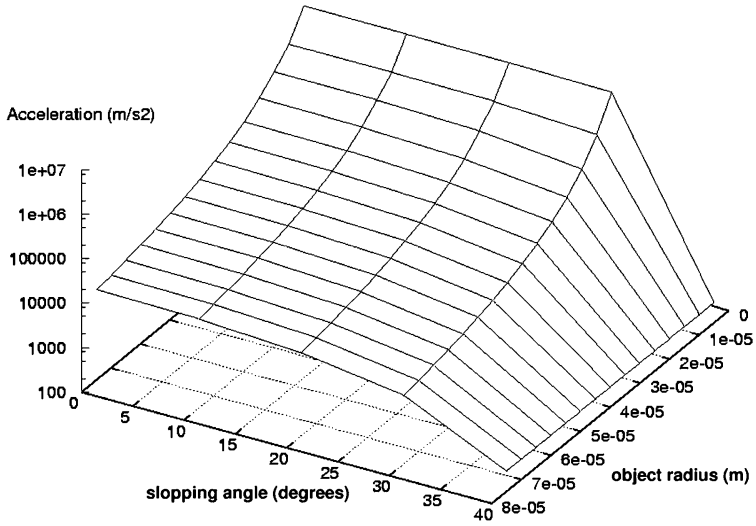

Figure 2. Minimum acceleration for the release of a glass sphere with a Si gripper.

3. ROLLING MODEL

Another way to release a spherical object is by reducing its adhesion force to the gripper. As the material properties cannot be changed, the only way to reduce the adhesion is reducing the contact area. It can be achieved by moving the object to the extremity of the tool. This motion makes it necessary to make the object roll or slide between the tool and the substrate. The switch between these two modes requires the control of normal and tangential load forces. An analytical model taking into account the adhesion forces and contact deformation is presented here. In this model (Fig. 3), the static equilibriums of the object and the tool are studied, including, at each interface $\mathcal{I}_{\text{os}}$ and $\mathcal{I}_{\text{ot}}$ (object/substrate and object/tool, respectively):

- adhesion forces of i on j $\vec{F}_{ij}^{\text{adh}}$, with $\vec{F}_{ij}^{\text{adh}} = -\vec{F}_{ji}^{\text{adh}}$ and $F_{ij}^{\text{adh}} = F_{ji}^{\text{adh}}$, perpendicular to the surface;
- normal force applied by i on j, $\vec{F}_{ij}^{\text{N}}$, with $\vec{F}_{ij}^{\text{N}} = -\vec{F}_{ji}^{\text{N}}$ and $F_{ij}^{\text{N}} = F_{ji}^{\text{N}}$, perpendicular to the surface; and
- friction force in the motion of j over i f_{ij}, with $\vec{f}_{ij} = -\vec{f}_{ji}$ and $f_{ij} = f_{ji}$, tangent to the surface.

Moreover, R is the sphere radius of the object, θ is the orientation error of the tool, which should be null in an ideal case and F_{ext} is the external force applied to the gripper. Rolling resistance moments are denoted M_{so} and M_{to}, and friction coefficients are μ_{so} and μ_{to}.

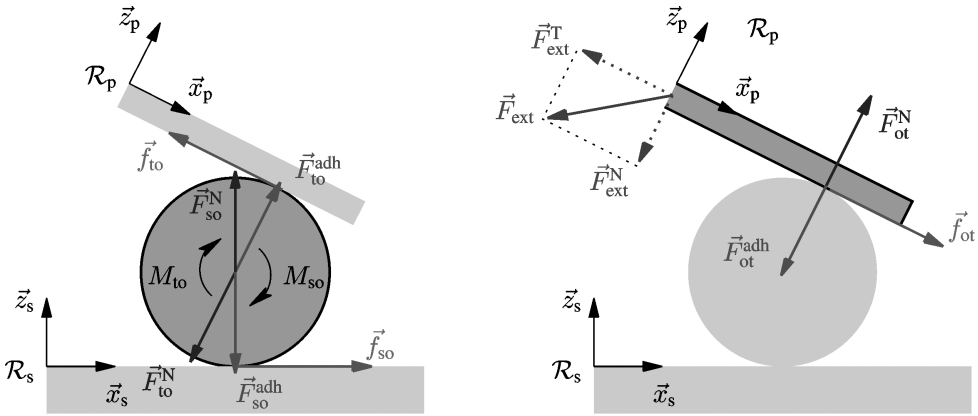

Figure 3. Static analysis of the rolling mode.

On the assumption of a quasi-static process [13], the following equilibrium equations are obtained:

$$\begin{cases} F^{N}_{so} - F^{adh}_{so} - F^{N}_{to}\cos\theta + F^{adh}_{to}\cos\theta + f_{to}\sin\theta = 0, \\ \qquad - F^{N}_{to}\sin\theta + F^{adh}_{to}\sin\theta + f_{so} - f_{to}\cos\theta = 0, \\ \qquad\qquad M_{so} + M_{to} - R(f_{so} + f_{to}) = 0. \end{cases} \tag{5}$$

The static equilibrium of the tool is written by projecting F_{ext} in $\mathcal{R}_p$:

$$\begin{cases} f_{ot} - F^{T}_{ext} = 0, \\ F^{N}_{ot} - F^{adh}_{ot} - F^{N}_{ext} = 0. \end{cases} \tag{6}$$

The modulus of adhesion forces F^{adh}_{so} and $^{adh}_{to}$ are bounded by pull-off forces given by JKR or DMT theories, as in (1).

$$\frac{3}{2}\pi R W_{so} \leqslant F^{adh}_{so} \leqslant 2\pi R W_{so}, \tag{7}$$

$$\frac{3}{2}\pi R W_{to} \leqslant F^{adh}_{to} \leqslant 2\pi R W_{to}. \tag{8}$$

Maugis [14] introduces the elasticity parameter λ, in order to choose the most appropriate contact model for a given case. For an interface between two bodies i and j this coefficient is expressed by:

$$\lambda_{ij} = 2\sigma_0\left(\frac{R}{\pi W_{ij} K^2}\right)^{1/3}, \tag{9}$$

$$F_{ij}^{\mathrm{adh}} = \begin{cases} 2\pi R W_{ij} & \text{for } \lambda_{ij} < 0.1, \\ \left(\dfrac{7}{4} - 1/4\dfrac{4.04\lambda^{1/4} - 1}{4.04\lambda^{1/4} + 1}\right)\pi W_{ij} R & \text{for } 0.1 < \lambda_{ij} < 5, \\ \dfrac{3}{2}\pi R W_{12} & \text{for } \lambda_{ij} > 5, \end{cases} \tag{10}$$

where K is the equivalent elastic modulus, calculated using the Poisson's ratio μ and Young's modulus E.

$$K = \frac{4}{3}\left(\frac{1-\mu_1^2}{E1} + \frac{1-\mu_2^2}{E2}\right),$$

W_{so} and W_{to} are work of adhesion for $\mathcal{I}_{\mathrm{so}}$ and $\mathcal{I}_{\mathrm{to}}$, respectively. W_{ij} can be calculated as $W_{ij} = \gamma_i + \gamma_j - \gamma_{ij} \simeq 2\sqrt{\gamma_i \gamma_j}$, where γ_{ij} interfacial energy, γ_i and γ_j surface energy of the object, substrate or tool [15].

The maximum rolling resistances are given by a linear function of the contact area [16, 17]. They are expressed by [18]:

$$M_{ij}^{\max} = C_{ij} W_{ij} a_{ij}, \tag{11}$$

where C_{ij} is the maximum rolling resistance coefficient and a_{ij} is the contact area radius between i and j. C_{ij} is considered a constant as a first approximation.

For different values of λ, the contact radius a_{ij} is then expressed by [14]:

$$a_{ij}^3 = \begin{cases} \dfrac{R}{K}\left(F_{ij}^{\mathrm{N}} + F_{ij}^{\mathrm{adh}}\right), & \text{for } \lambda_{ij} < 0.1, \\ a_0^3\left(\dfrac{\alpha + \sqrt{1 + F_{ij}^{\mathrm{N}}/F_{ij}^{\mathrm{adh}}}}{1+\alpha}\right)^3, & \text{for } 0.1 < \lambda_{ij} < 5, \\ \dfrac{R}{K}\left(\sqrt{F_{ij}^{\mathrm{N}} + F_{ij}^{\mathrm{adh}}} + \sqrt{F_{ij}^{\mathrm{adh}}}\right), & \text{for } \lambda_{ij} > 5, \end{cases} \tag{12}$$

with α and a_0^3 obtained by:

$$\lambda_{ij} = -0.924\ln(1 - 1.02\alpha) \quad \text{and} \quad a_0^3 = \left(1.54 + 0.279\frac{2.28\lambda_{ij}^{1/3} - 1}{2.28\lambda_{ij}^{1/3} + 1}\right)^3 \frac{\pi W_{ij} R^2}{K}. \tag{13}$$

3.1. Sliding conditions

Sliding conditions for $\mathcal{I}_{\mathrm{so}}$ and $\mathcal{I}_0$ are expressed as a function of the normal force applied to the microsphere by the tool, respectively:

$$f_{\mathrm{so}} \geqslant \mu_{\mathrm{so}} F_{\mathrm{so}}^{\mathrm{N}}, \tag{14}$$

$$f_{\mathrm{to}} \geqslant \mu_{\mathrm{to}} F_{\mathrm{to}}^{\mathrm{N}}. \tag{15}$$

(5) and (6) are then used to define friction and normal forces in (14) and (15):

$$\begin{cases} f_{\mathrm{so}} = -F_{\mathrm{ext}}^{\mathrm{N}} \sin\theta - F_{\mathrm{ext}}^{\mathrm{T}} \cos\theta, \\ F_{\mathrm{so}}^{\mathrm{N}} = F_{\mathrm{os}}^{\mathrm{adh}} + F_{\mathrm{ext}}^{\mathrm{N}} \cos\theta - F_{\mathrm{ext}}^{\mathrm{T}} \sin\theta, \end{cases} \quad \text{and} \quad \begin{cases} f_{\mathrm{to}} = -F_{\mathrm{ext}}^{\mathrm{T}}, \\ F_{\mathrm{to}}^{\mathrm{N}} = F_{\mathrm{ext}}^{\mathrm{N}} + F_{\mathrm{ot}}^{\mathrm{adh}}. \end{cases} \tag{16}$$

Using (14), condition on the external force for sliding at $\mathcal{I}_{\mathrm{so}}$ can be written as:

$$F_{\mathrm{ext}}^{\mathrm{T}} \geqslant \frac{\mu_{\mathrm{so}} F_{\mathrm{so}}^{\mathrm{adh}} + (\mu_{\mathrm{so}} \cos\theta - \sin\theta) F_{\mathrm{ext}}^{\mathrm{N}}}{\cos\theta + \mu_{\mathrm{so}} \sin\theta} = F_{\mathrm{cs}}. \tag{17}$$

Identically, for sliding at $\mathcal{I}_{\mathrm{ot}}$ (15) is:

$$F_{\mathrm{ext}}^{\mathrm{T}} \geqslant \mu_{\mathrm{to}} \left(F_{\mathrm{ext}}^{\mathrm{N}} + F_{\mathrm{to}}^{\mathrm{adh}} \right) = F_{\mathrm{ct}}. \tag{18}$$

The critical values are hereafter referred to as F_{cs} or F_{ct} for tool–side and substrate–side interfaces, respectively.

3.2. Rolling conditions

Rolling conditions imply that the rolling resistance generated at each contact interface simultaneously exceeds the maximum rolling resistance on the interface. Assuming that the maximum rolling resistance is proportional to the contact radius [17], equation (5) gives the rolling resistance:

$$M_{\mathrm{so}} = \frac{a_{\mathrm{so}}}{a_{\mathrm{so}} + a_{\mathrm{to}}} R(f_{\mathrm{so}} + s_{\mathrm{to}}) \quad \text{and} \quad M_{\mathrm{to}} = \frac{a_{\mathrm{to}}}{a_{\mathrm{so}} + a_{\mathrm{so}}} R(f_{\mathrm{so}} + f_{\mathrm{to}}). \tag{19}$$

Both inequalities should be satisfied simultaneously for the microsphere to roll:

$$\begin{cases} M_{\mathrm{so}} \geqslant M_{\mathrm{so}}^{\max} = c_{\mathrm{so}} W_{\mathrm{so}} a_{\mathrm{so}}, \\ M_{\mathrm{to}} \geqslant M_{\mathrm{to}}^{\max} = c_{\mathrm{to}} W_{\mathrm{to}} a_{\mathrm{to}}. \end{cases} \tag{20}$$

Using equations (11) and (16), both inequalities can be expressed as:

$$\begin{cases} F_{\mathrm{ext}}^{\mathrm{T}} \geqslant \dfrac{c_{\mathrm{so}}(a_{\mathrm{so}} + a_{\mathrm{to}}) W_{\mathrm{so}} - R F_{\mathrm{ext}}^{\mathrm{N}} \sin\theta}{R(1 + \cos\theta)}, \\ F_{\mathrm{ext}}^{\mathrm{T}} \geqslant \dfrac{c_{\mathrm{to}}(a_{\mathrm{so}} + a_{\mathrm{to}}) W_{\mathrm{to}} - R F_{\mathrm{ext}}^{\mathrm{N}} \sin\theta}{R(1 + \cos\theta)}, \end{cases} \tag{21}$$

or, combining these two equations into one:

$$F_{\mathrm{ext}}^{\mathrm{T}} \geqslant \frac{(a_{\mathrm{so}} + a_{\mathrm{to}}) \max\{c_{\mathrm{so}} W_{\mathrm{so}}, c_{\mathrm{to}} W_{\mathrm{to}}\} + R F_{\mathrm{ext}}^{\mathrm{N}} \sin\theta}{R(1 + \cos\theta)} = F_{\mathrm{cr}}. \tag{22}$$

Similarly to the sliding case, the critical value for rolling F_{cr} is introduced here.

The motion of the object between the gripper and the substrate depends on which of the critical forces F_{cr}, F_{ct}, F_{cs} is first reached by the tangential force $F_{\mathrm{ext}}^{\mathrm{T}}$. All three values can be controlled through the normal load $F_{\mathrm{ext}}^{\mathrm{N}}$. According to the comparative magnitudes of F_{cr}, F_{ct}, F_{cs}, the microsphere behaviour can be classified into three modes:

(1) $F_{\text{ext}}^{\text{T}} \geqslant F_{\text{cs}} = \min\{F_{\text{cs}}, F_{\text{ct}}, F_{\text{cr}}\} \Rightarrow$ sliding on the substrate–side interface S_{s};

(2) $F_{\text{ext}}^{\text{T}} \geqslant F_{\text{ct}} = \min\{F_{\text{cs}}, F_{\text{ct}}, F_{\text{cr}}\} \Rightarrow$ sliding on the tool–side interface S_{t};

(3) $F_{\text{ext}}^{\text{T}} \geqslant F_{\text{cr}} = \min\{F_{\text{cs}}, F_{\text{ct}}, F_{\text{cr}}\} \Rightarrow$ rolling.

Note that the use of the $\geqslant$ sign implies an accelerating motion if the external force is actually greater. Practically, the gripper's actuators easily develop forces higher than slide/roll limits, but the horizontal motion can generally be controlled for constant speed, which implies $\sum F = 0$.

3.3. Simulation and analysis

In order to illustrate the rolling and sliding modes, a numerical simulation is proposed. The chosen configuration is a Teflon substrate, a polystyrene object with a radius of 20 μm and a silicon tool. This choice is motivated by the weak adhesion between Teflon and polystyrene. This would allow to simulate the gripping of the object by adhesion, and its release on the same substrate by rolling. Table 1 gives the numerical values for some parameters [19].

The Dugdale coefficient λ is calculated accordingly:

- substrate–object interface: $\lambda = 0.065\ \mu$m
- tool–object interface: $\lambda = 2.53\ \mu$m.

The rolling resistance coefficient C_{ij} is not a well-defined value, in the literature it is generally assumed to be $10^{-4} < C_{ij} < 10^{-5}$ [20]. We have chosen $C_{\text{os}} = C_{\text{ot}} = C$ for the simulations.

Following the curves in Fig. 4 gives F_{cr}, F_{ct}, F_{cs} for applied normal load F_{N}. The switch between rolling and sliding occurs when their relative magnitude changes. The influence of the variation of parameters such as orientation error θ, subtrates surface energy γ_s and the rolling resistance c is also studied.

Following remarks can be made based on the simulation results:

- The sliding of the object on the gripper can only be observed if the subtrate adhesion is higher than the gripper adhesion. As this would not allow an adhesion-based gripping, this mode is never observed.
- There is a minimum amount of normal force necessary to guarantee the rolling. Therefore, considering that both the gripper and the object may be fragile, it

Table 1.
material properties

	Silicon	Polymer	Teflon
Work of adhesion (mJ/m^2)	1400	35.5	18
Poisson's ratio	0.17	0.39	0.46
Young's modulus (GPa)	140	3.4	0.5
Maximum friction coefficient	0.25	0.1	0.1

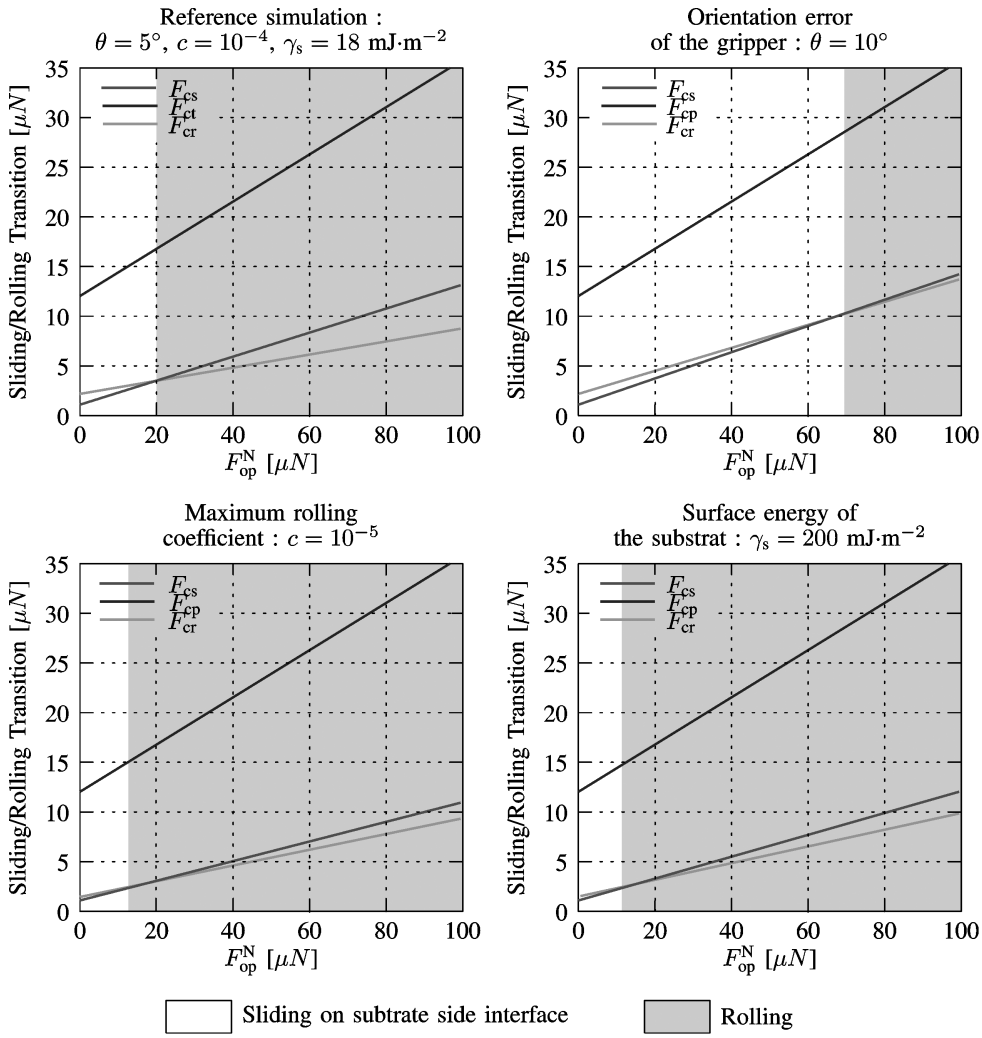

Figure 4. Influence of various parameters on sliding/rolling behaviour. Simulation results.

is necessary to control this force precisely. This would also allow a controlled switch between sliding and rolling modes for precise positioning.

- Slipping occurs if the normal force is less than a minimal value.
- The orientation error θ has a significant effect. The increase from 5 to 10 causes a significant reduction on the rolling area. This angle should be kept as low as possible for a controlled rolling experiment.
- The maximum parameter of rolling C is badly known, as it can only be empirically evaluated. Its influence is clearly visible in the switch between the rolling and sliding modes. An interesting approach is to use a perfectly calibrated system, consisting of θ, W_{os} and W_{og} with controlled load F^{ext}, and the only

unknown parameter is C. It would be then possible to measure its value based on the mode switch critical load.

This theoretical approach is experimentally validated using [*mü*]MAD, our micromanipulation system. Moreover, it requires precise control of contact force and motion, in both normal and tangential axis.

4. EXPERIMENTAL CONFIGURATION

The micromanipulation system developed in our lab is built around an active gripper, whose design is based on the adhesion phenomena. According to the study presented above, it includes two important capabilities: high acceleration generation for dynamical release and precise contact force control for rolling. This gripper is an AFM (atomic force microscopy) tipless cantilever beam (from NanoSensor), mounted on a piezoelectric ceramic which can produce impulses or high frequency sinusoidal waves, generating instantaneous accelerations as high as 10^6 m/s^2 at the extremity of the AFM cantilever. These outstanding dynamical capabilities are used for release and characterisation tasks. The gripper also provides μN resolution measurement of the contact force, due to the AFM probe. Its vertical displacement is provided by two serial actuators: a nanostage with 12 μm amplitude (from Physik

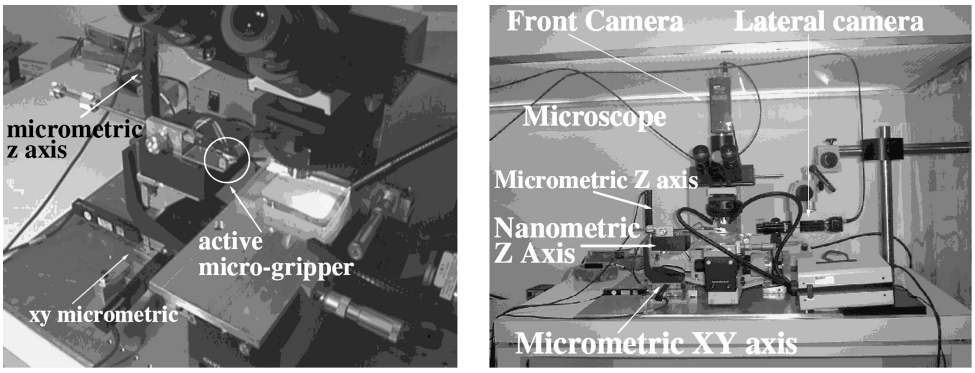

Figure 5. Micromanipulation system.

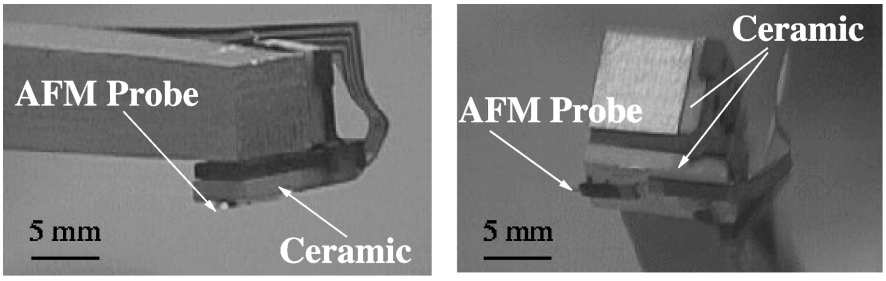

Figure 6. The active gripper.

Instrument) and a microstage (from Newton Microcontrol) with sub-micrometer resolution over 2.5 cm. The contact force is, thus, controlled by the motion of these actuators. The horizontal motion is produced by two identical microstages. Figure 5 shows the whole micromanipulator, called [*mü*]MAD, placed under an optical microscope. The active gripper is shown in Fig. 6.

5. CONTROL IMPLEMENTATION

For autonomous manipulation, the motion of the gripper must be controlled with precision. Moreover, the contact force control is very important when handling fragile microparts and, as seen in the previous section, an absolute necessity for the proposed rolling release mode. For the motion in the horizontal plane, visual servoing based on the microscope top-view is used. For vertical motion, due to the very small depth of the field of the microcope image, a focus-based control is implemented. Force control uses the gripper's measurement capabilities with both vertical actuators, the nanostage and the microstage.

5.1. Motion of the gripper on horizontal plane

Position servoing of the gripper on the horizontal plane is done by image-based visual servoing using an external camera, described in Fig. 7. In this case, the problem is simplified for two reasons. First, the robot has no rotational joints; therefore, classical difficulties of visual servoing are eliminated. Moreover, the plane defined by the x and y axes of the microstage is almost parallel to the microscope image plane, so that once the image is focused on the gripper, its appearance should be identical, regard less of its motion along the x and y axes. That is why it is enough to process only a single point. Thus, the goal is to reduce the error $(\epsilon_x\ \epsilon_y)$ between the gripper contact point desired position $(u^* v^*)$ and its actual position (uv) in the current image (i.e., expressed in pixel coordinates) by appropriately moving it in the workspace.

5.1.1. Template extraction. Before processing, a sub-image taken from a focused image, containing the final part of the gripper is extracted. Contours are detected

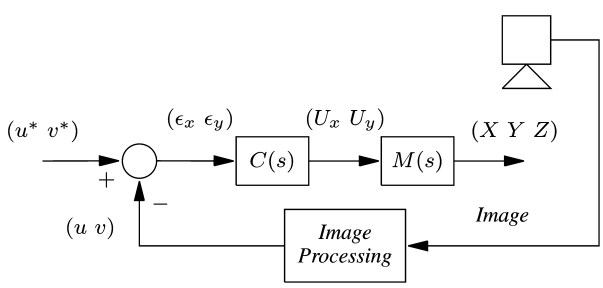

Figure 7. Image-based visual servoing scheme.

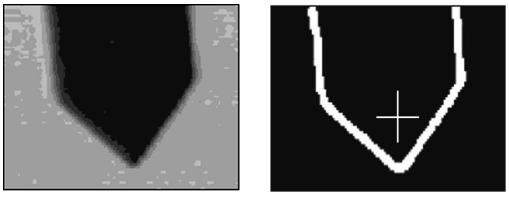

Figure 8. End-effector sub-image and template.

using Sobel masks, as explained in Section 5.2.1. The output image is the template of the gripper. The operator must specify the desired contact point along the main axis of symmetry. Figure 8 illustrates a typical template with its contact point.

5.1.2. Real-time detection. The gripper contact point has to be known in each acquired image. This is done by a template matching method. Assuming that the algorithm knows the position of the template in the previous image, the template will be searched for an extended area compared to the template sub-image. This area of interest is first processed like the template, and then swept and compared pixel by pixel to determinate its best matching location according to a vote process. Knowing the template position in the image, the current position of the contact point is deduced.

5.1.3. Performance. Even if the static error of this servoing is null, there is a remaining uncertainty about the absolute position of the gripper, which depends on the real area size covered by a pixel (i.e., on the zoom). In our case, this uncertainty is about 2 cm, which is not very accurate, but it is now stabilized with respect to the vertical motion of the gripper. Indeed, if the optical and motion axes are not perfectly aligned, the induced deviation is permanently corrected (for an alignment error of 1 degree and a vertical motion of 1 mm, the gripper would deviate by more than 17 μm).

5.2. Focusing

The goal of an autofocus algorithm is to find the appropriate camera position so that a part of the image is focused. Focus perception is not an absolute criterion. However, some image properties are affected by good or bad focus and can be used to build suitable criteria. Among these observations, we can say that focused images have more high-frequency components, more localised histograms, higher contrast, higher peaks and deeper valleys than blurred images. The goal of an autofocus algorithm is to find the appropriate camera position so that a part of the image is focused. With a criterion based on one of these properties, the focusing problem can be processed as an optimisation problem. A convenient criterion must:

- have an optimum corresponding to the best focused image;
- have a thin peak (or valley) around the optimum;

- have a high peak (or deep valley) around the optimum;
- not have local optima.

5.2.1. Criterion choice. The ability for a criterion to satisfy these conditions depends a lot on the features included in the image and the recording conditions. In the current case, images have two types of features: gripper and/or objects. Moreover, recording conditions, mainly the lighting, are steady because of working in a controlled environment (clean-room). For this reason, our criterion does not need to be highly adaptive to be efficient. Once criterion parameters are fixed in the experimental conditions, the algorithm should work.

Some simple criteria have been tested, one of which was chosen for quantification of high-frequency components of the image. For an image I_z, taken by a camera at position z, of width N and height M, the criterion is written as:

$$f(z) = \frac{1}{NM} \sum_{i=1}^{N-2} \sum_{j=1}^{M-2} \sqrt{|G_x(i,j)|^2 + |G_y(i,j)|^2}, \tag{23}$$

where G_x and G_y are the convolution of the initial image I_z with horizontal and vertical Sobel masks, respectively.

$$S_x = \begin{bmatrix} -1 & 0 & 1 \\ -2 & 0 & 2 \\ -1 & 0 & 1 \end{bmatrix} \quad \text{and} \quad S_y = \begin{bmatrix} -1 & -2 & -1 \\ 0 & 0 & 0 \\ 1 & 2 & 1 \end{bmatrix}.$$

Moreover, gradients are summed in (23) only if they are lower than a threshold fixed experimentally in order to eliminate noise in the measurement. Another consequence is that f is exactly null for blurred images, so that the exploration direction of the optimisation process is not affected at all by noise when the camera is far from its optimal position. Figure 9 illustrates a measure of focus versus camera position, using the described criterion and Fig. 10 gives images of the gripper taken at various distances from the optimal position. Notice that it is not easy for a human being to differentiate, for example, between images (i) and (ii), whereas the algorithm does.

5.2.2. Autofocus experiment. Under practical conditions, the operator must first specify an area of interest containing the blurred gripper or objects in the image, and then initialise the exploration direction. The camera moves along its optical axis at constant speed, while the focus criterion is null. When the criterion becomes non-null, the desired camera motion speed is computed as:

$$v_c^* = K \Delta_n f, \tag{24}$$

where K is the gain and $\Delta_n f$ is the average slope of f computed off the last n measures. The problem of choosing an initial direction of exploration can be solved assuming that the relative positions of focal plane, gripper plane and object plane are known at an initial state where all vertical axes are at their bounds.

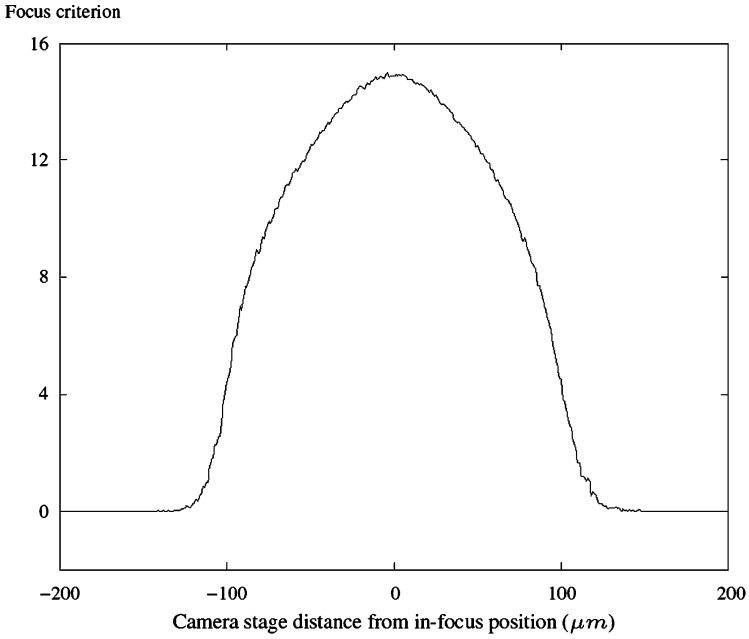

Figure 9. Focus criterion measure.

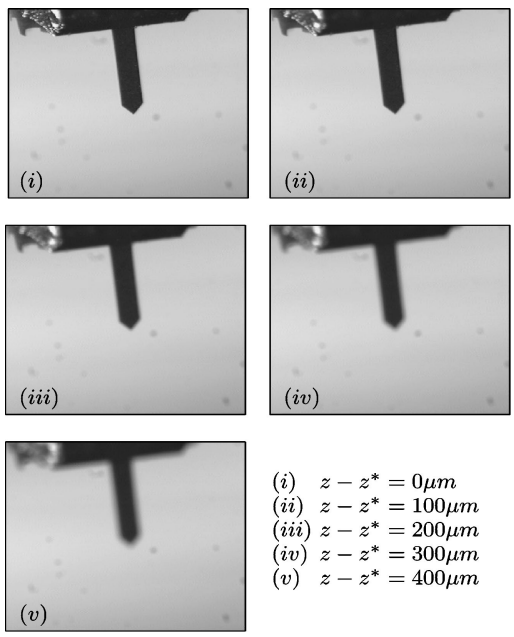

Figure 10. Images of the gripper taken at various distances from the optimal focused position z^*.

5.3. Force measurement

The gripper is an AFM (atomic force microscopy) tipless cantilever beam (see Fig. 11). It is a built-in silicon rectangular prism, $600 \times 140 \times 10$ cm^3 in size, where E and L are the Young's modulus and inertia momentum, respectively. Its deflection is measured by piezoresistivity through a Wheatstone bridge placed at the built-in end.

5.3.1. Modeling. The output signal from this kind of piezoresistive cantilever is generally written as:

$$U = A_U \omega(\delta) + U_0 \quad \text{or} \quad U = A'_U \varepsilon(\delta) + U_0, \tag{25}$$

where U is the output voltage, A_U or A'_U the overall amplification gain and U_0 the measure offset. $\omega(\delta)$ and $\varepsilon(\delta)$ are the rotation of the section and the local strain at δ from the built-in end, where the piezoresistive gauge is placed, respectively. Under the Bernouilli hypothesis for bending beams, ω can be written as:

$$\omega_l(x) = \frac{\mathrm{d}v_l}{\mathrm{d}x} = \left(lx - \frac{x^2}{2}\right)\frac{F_l}{EI}, \tag{26}$$

where v_l and F_l are, respectively, the deflection and applied force at distance l from the built-in end, with:

$$u_L = \frac{F_L L^3}{3EI} = \frac{F_L}{K_\mathrm{s}} \quad \left(\Rightarrow K_\mathrm{s} = \frac{3EI}{L^3}\right). \tag{27}$$

Hence, assuming $\delta \ll L(L/\delta) > 100$), and using (27), $\omega(\delta)$ can be written as:

$$\omega(\delta) = \frac{3l\delta}{L^3} v_L. \tag{28}$$

Similarly, the strain $\varepsilon(\delta)$ can be calculated using Hook's law from:

$$\varepsilon(\delta) = \frac{\sigma}{E} = \frac{3E(L-\delta)h}{2L^3} v_L \simeq \frac{3E(L)h}{2L^3} v_L. \tag{29}$$

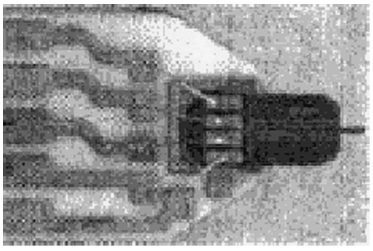

Figure 11. Force measurement device.

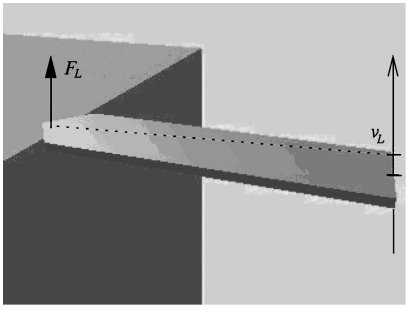

Figure 12. Calibration configuration.

Both (28) and (29) lead to a linear relation between the measured voltage U and the deflection v_L:

$$U = A_U \frac{3l\delta}{L^3} v_L + U_0 = A'_U \frac{3E(L)h}{2L^3} v_L = K_U v_L + U_0. \tag{30}$$

As both A_U and A'_U depend on the characteristies of the piezoresistor and are very diffucult to quantify, it is necessary to calibrate K_U (and U_0) experimentally. This equation can be interpreted as:

$$v_L = \frac{U - U_0}{K_U}, \tag{31}$$

and for the applied force:

$$F_L = K_s \frac{U - U_0}{K_U}. \tag{32}$$

The value of K_s is given by the constructor of the AFM probe, as $K_s = 21.06$ N/m^2. It has also been studied by finite elements (CASTEM software) and verified by vibrational analysis.

5.3.2. Calibration. The deflection of the cantilever can be measured by touching its end to a rigid surface. The induced deformation is directly opposite to the nanostage position from the initial contact point. As the nanostage has 3 nm precision, very accurate measurements are possible. In manipulation conditions, objects are gripped in $l < L$ in order to ensure contact. In this case, (31) and (32) actually give the equivalent theoretical applied force F_L^*, and the induced theoretical deflection v_L^*. The output signal U will be the same if the force F_l applied at the distance l is the same as the moment from the force F_L^* applied at L. Considering $L \gg \delta$ as before,

$$F_l \cdot l = F_L^* \cdot L \Rightarrow \frac{F_l}{F_L^*} = \frac{L}{l}. \tag{33}$$

Table 2.
Verification of equation (35)

Contact point ratio (l/L)	1 : 2	3 : 4	1 : 1
Measured deflection v_l (μm)	0.65	1.50	2.48
Ratio $\left(\frac{v_l}{v_L}\right)/\left(\frac{l}{L}\right)^2$	1.048	1.075	1.000

Thus, knowing the contact point l, and measuring the voltage U, the real applied force is

$$F_l = K_s \frac{L}{l}\left(\frac{U - U_0}{K_U}\right). \tag{34}$$

In the same way as for (34), but using (27), we obtain that

$$\frac{v_l}{v_L^*} = \left(\frac{l}{L}\right)^2, \tag{35}$$

thus, the real deflection at contact point l is

$$v_l = \left(\frac{l}{L}\right)^2 \left(\frac{U - U_0}{K_U}\right). \tag{36}$$

5.3.3. Validation. In order to validate (35), and the theoretical results of Section 5.3.2, we calibrated at different contact points and measured the variation of the nanostage position between the initial contact position and the position required to produce a fixed voltage output. The results are collected in Table 2. The fact that the ratio of the deflection ratio by the squared contact point ratio on the third line of Table 2 is steadily equal to unity proves that, knowing the ratio l/L using vision, we are able to improve rough measures provided by the calibration using (34) and (36).

5.3.4. Experimental measures. Figure 13 shows a pull-off force measure. Initially, the extremity of the gripper is in contact with the substrate and applies a force higher than 50 μN. Then, the gripper is moved up at constant speed of 500 nm/s. The measured applied force decreases to zero, when the beam deflection is null. Afterwards, as the gripper moves upwards, the measured force becomes negative: the contact between the extremity of the gripper and the substrate is kept until the elastic force accumulating in the gripper overweights the pull-off force. In this case the measured magnitude is 18.23 μN.

5.4. Force servoing

To bring the gripper in contact with the desired object, an accurate interaction force control is needed. The vertical motion of the gripper can be done in two complementary stages described in Table 3. The given induced force resolution

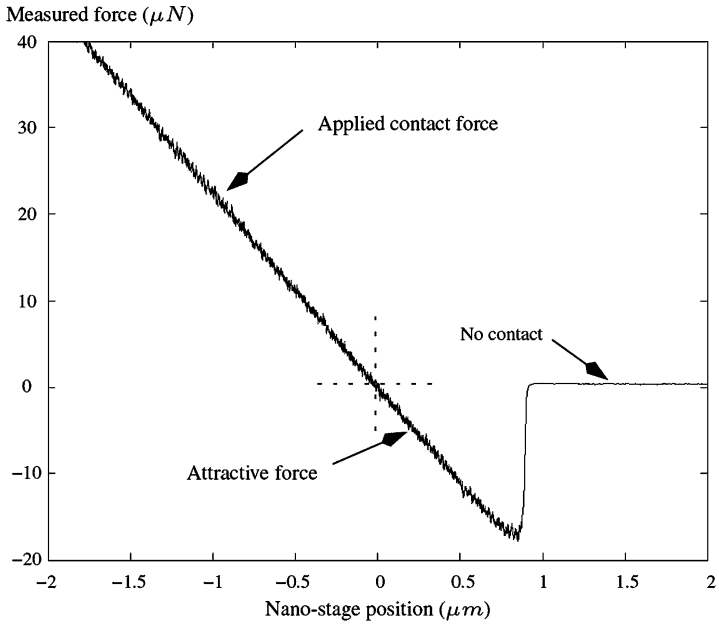

Figure 13. Pull-off measure.

Table 3.
Vertical axis specification

Axis type	Micro	Nano
Travel range (μm)	25×10^3	12
Travel resolution (nm)	50	2
Induced force range (μN)	526.5×10^3	252.72
Induced force resolution (nN)	1.053×10^3	42.12
Loop period limitation (ms)	40	—

is theoretical because it is only computed from the travel range resolution. In practice, in-line voltage measurement noise reduces this resolution, but filtering can improve it for off-line data analysis. The loop period limitation is due to the fact that the micro-stage is controlled by a deported serial-linked computer whose communication speed is fixed at video rate.

5.4.1. Basic loop. A basic force servoing loop has been implemented to control the nano-translator stage, thus the gripper is able to apply a precise contact force. Figure 14 shows the force control scheme. F^* and F are the desired and measured force, ϵ_n is the servoing error, U_n the input voltage and z_n the nano-translator position,

$$N(s) = \frac{1.585 \times 10^6}{s(s^2 + 2.508 \times 10^3 s + 1.310 \times 10^6)}$$

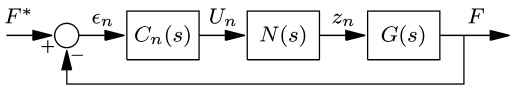

Figure 14. Basic force servoing loop scheme.

the transfer function of the low-level-controlled nanometric stage, $G(s)$ the transfer function of the beam and $C_n(s)$ the corrector term. Assuming that the deflection of the beam v_l is the opposite of the nano-stage position z_n measured from its initial contact position z_n^0, and using (34) and (36), we deduce that

$$F = \begin{cases} 0, & \text{if } z_n \geqslant z_n^0, \\ \underbrace{K_s\left(\dfrac{L}{l}\right)^3}_{K_s}\left(z_n^0 z_n\right), & \text{if } z_n \leqslant z_n^0 \end{cases}. \tag{37}$$

Since we use a proportional corrector, $C_n(s) = K_n$, and considering the end-effector and object in contact, the transfer function of the system can be written as

$$H_f(s) = \frac{K_n K_g N(s)}{1 + K_n K_g N(s)}. \tag{38}$$

Owing to its travel range of 12 μm, the nano-stage may easily reach its bounds. Moreover, the end-effector should be very close to the object (a few micrometers) before starting the servoing in order to keep as much travel range as possible. However, this is not possible due to the inaccuracy of the position information given by focusing.

5.4.2. Enhanced loop. The way to solve this problem is to associate an auxiliary loop controlling the micro-stage with the basic one, whose goal is to maintain the nano-stage in the middle of its travel range. Due to their different resolutions, it is important to define a dead zone around the desired nano-stage position where the auxiliary loop has no effect in order to avoid undesirable oscillations. Figure 15 illustrates the overall servoing scheme.

When a contact force F^* is desired and the measured force F is null, the nano-stage reaches its bottom boundary due to the fast loop, and moves out of the dead zone. Consequently, the micro-stage moves down thanks to the auxiliary slow loop. When the gripper reaches the object, a non-null contact force is measured and the former loop works in linear mode. The secondary loop will stop when the nano-stage is in the dead zone and activate again if a new force command makes the nano-stage go out of the dead zone.

The full system can be described by the MIMO (Multi-Input/Multi-Output) transfer function

$$H(s) = \begin{bmatrix} H_{zz}(s) & H_{zf}(s) \\ H_{fz}(s) & H_{ff}(s) \end{bmatrix}, \tag{39}$$

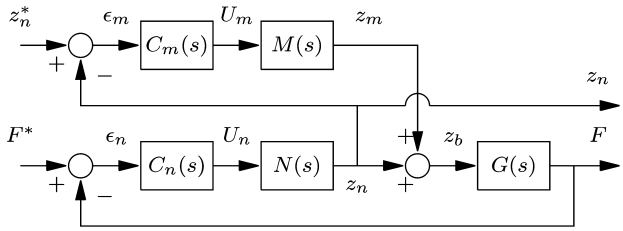

Figure 15. Enhanced force servoing loop scheme.

where (omitting to write dependencies on the variable s)

$$H_{zz} = \frac{-C_n C_m G N M}{1 + G C_n N - G C_n C_m N M},$$
$$H_{fz} = \frac{C_n N}{1 + G C_n N - G C_n C_m N M},$$
$$H_{zf} = \frac{G C_m M}{1 + G C_n N - G C_n C_m N M},$$
$$H_{ff} = \frac{G C_n N (1 - C_m M)}{1 + G C_n N - G C_n C_m N M},$$

with two switch conditions. The first one, about contact or not, is defined by (37). The second one depends on the threshold z_s of the dead zone of the auxiliary loop according to

$$\epsilon_m = \begin{cases} z_n^* - (z_n + z_s), & \text{if } z_n^* - z_n \geqslant z_s, \\ 0, & \text{if } |z_n^* - z_n| \leqslant z_s, \\ z_n^* - (z_n - z_s), & \text{if } z_n^* - z_n \leqslant -z_s. \end{cases} \tag{40}$$

5.4.3. Impact and contact force experiment. Figure 16 shows experimental results of the enhanced force servoing in two cases. In first one (Fig. 16a), the gripper has been placed above an object using vision focusing and servoing. Then it is asked to touch the object. The desired impact force is 50 μN. The observed overshoot depends on the speed limit of the microstage and the length of dead zone. It could be reduced by reducing the speed and increasing the dead zone, but consequently, the system would be slower and less reactive. In the second case (Fig. 16b), the gripper and the object are in contact and several desired contact forces are required.

5.5. Mode detection

The analysis of rolling experiment could be interesting for estimating micromechanical properties of the manipulated object. This requires to know the motion of the object during the release task. Let us rewrite (36), omitting the voltage offset, considering that U is null at no-load and assuming that the deflection at contact

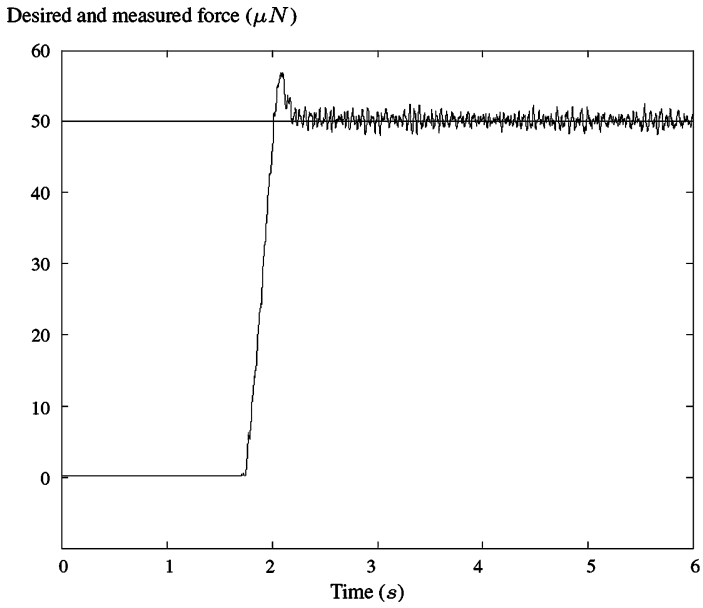

(a)

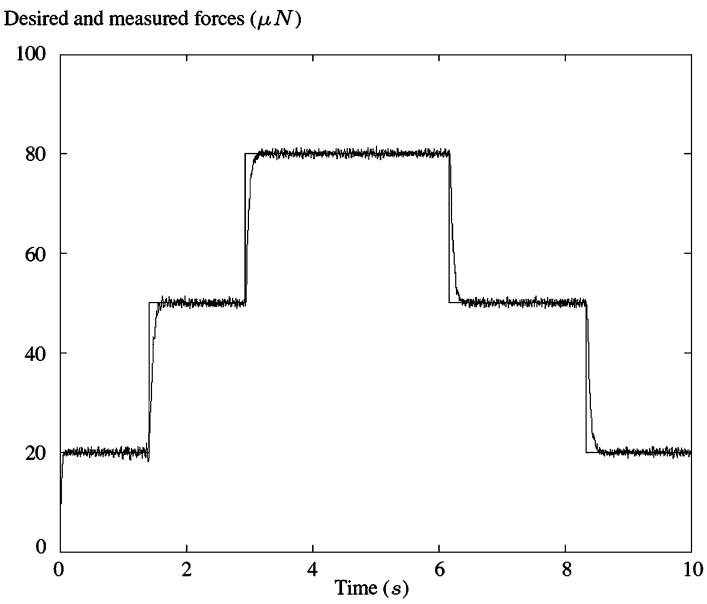

(b)

Figure 16. Impact (a) and contact (b) force control experiments.

point v_l is directly the opposite of the nano-stage position z_n, measured from the initial contact position z_n^0. Let us introduce the variable $z = z_n^0 - z_n$. The contact point is

$$U(t) = K_U \left(\frac{L}{l(t)}\right)^2 z(t) \Rightarrow l(t) = L\sqrt{K_U \frac{z(t)}{U(t)}}. \tag{41}$$

Comparing the variation of l with the gripper vertical motion, we are able to detect the current mode.

5.5.1. Instantaneous variations. From the partial derivative of (41), variations of Δl and Δz from an initial state (l_0, z_0) produce a variation of the measure

$$\Delta U = K_U \left(\frac{L}{l_0}\right)^2 \left(\Delta z - 2z_0 \frac{\Delta l}{l_0}\right). \tag{42}$$

The servoing loop described in Section 5.4.1 works on the voltage measure U, which is proportional to the applied force F for a steady contact point, so that this is really a force servoing loop. However, by running that loop here, it is possible to move the nano-stage by Δz to compensate the variation Δl in order to keep ΔU null. In this case, the contact point variation can be estimated as

$$\frac{\Delta l}{l_0} = \frac{\Delta z}{2z_0}. \tag{43}$$

The induced force variation is described, using (34), by

$$\frac{F_l}{F_{l_0}} = 1 - \frac{\Delta l}{l_0}. \tag{44}$$

As $\Delta l \ll l_0$, this variation should not produce a mode switch.

6. EXPERIMENTAL RESULTS

Figure 17a illustrates an autonomous pick-and place operation of a 50 μm glass object from the top view camera. Figure 17b shows the release by rolling phase from the side view camera. The evolutions of the nanostage z_n, measured voltage of the AFM beam U and the contact point displacement ratio l/L are represented in Figs 18 and 19.

In Fig. 18 the gripper's motion along the X axis starts at $t = t_1$. As the force servoing is activated, the measured voltage U is steady until the release at $t = t_2$. As the object rolls towards the beam's extremity, the nano-stage moves down to keep the contact force constant. Between $t = t_2$ and $t = t_3$, the contact point follows the curve of the object until complete separation at t_3. The rolling distance to beam length ration l/L is estimated using equation (41). As it can be also seen in Fig. 19, the nano-stage motion is not completely linear: the object does not roll continuously,

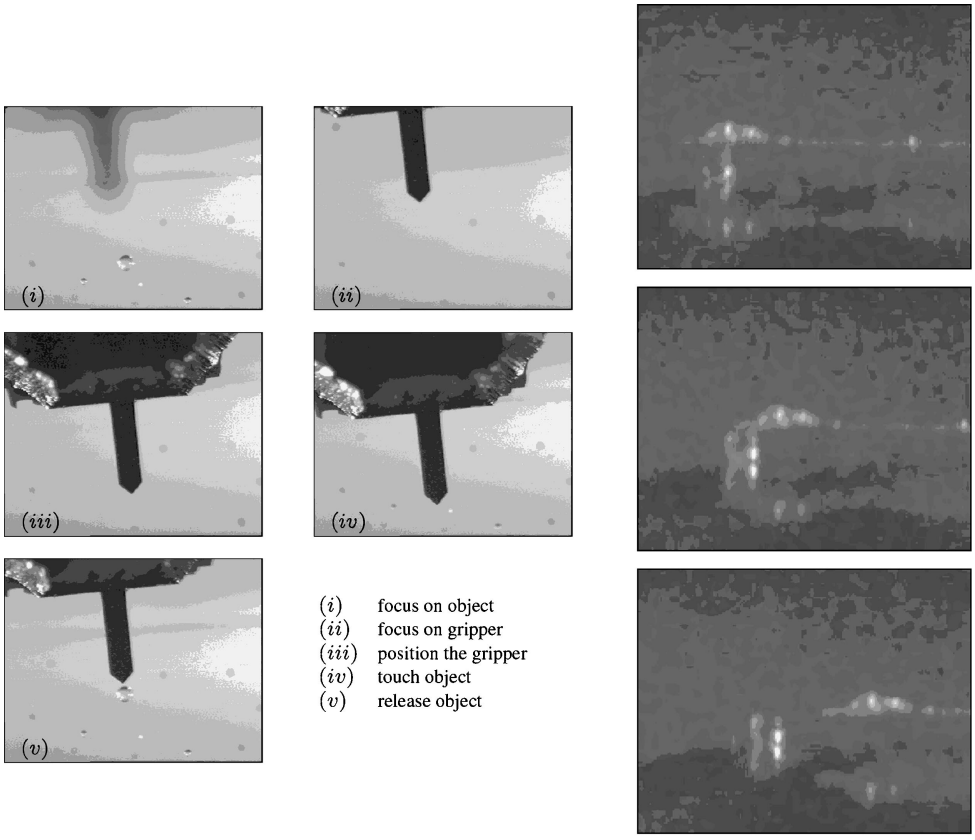

(a) Top view (b) Side view of release phase

Figure 17. Complete pick-and-place experiment with vision and force control. Each phase, pick-up or release, takes less than 1 min.

due to the irregularities on the substrate's or the gripper's surfaces. The observed mode is rather a mixture of rolling and sliding. However, the proposed system allows to track the objects motion based on l/L ratio from the gripper's output.

7. CONCLUSIONS

This paper describes a release strategy for microobjects gripped by adhesion. This rolling-release method adds to adhesion based gripping and static and dynamic release modes already integrated to our micromanipulator [*mü*]MAD. First, the proposed release mode is explored theoretically. This analysis allowed to define some conditions on contact forces between the gripper, the manipulated object and the substrate, in regards to adhesion and friction forces.

Therefore, in order to experiment this proposed release mode, vision and force feedback techniques that allow to achieve accurate and safe autonomous microma-

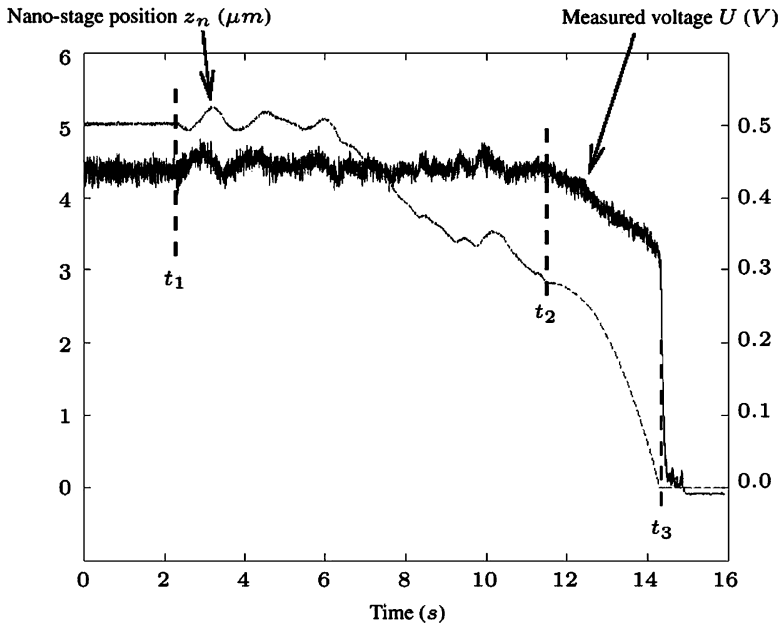

(a)

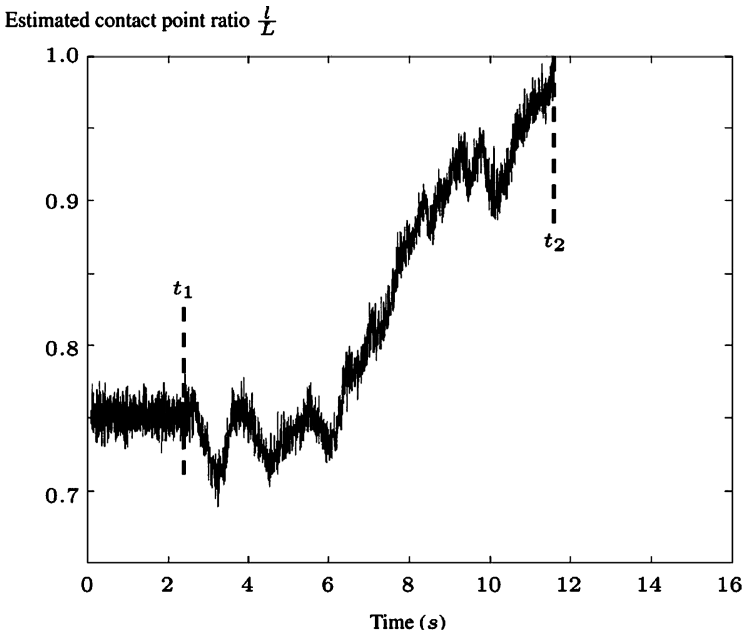

(b)

Figure 18. Rolling experiment (1): Force measures, nanostage motion and contact point estimation.

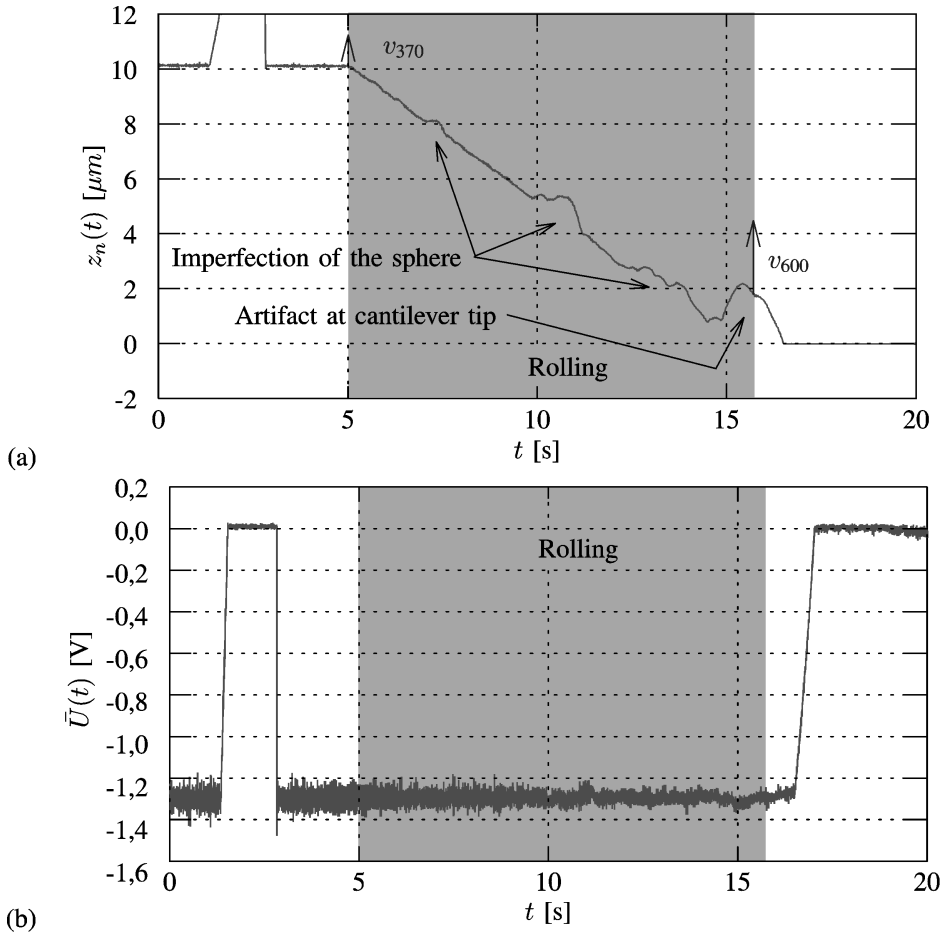

Figure 19. Rolling experiment (2): Evolutions of nanostage position (a) and output of AFM probe (b).

nipulation are established. 3D vision servoing uses tracking on the x–y plane and focus information on the z axis.

Force servoing takes advantage of the kinematic redundancy of two actuators, one with large range and the other with small range and nanometric precision. The designed scheme allows precise control of the impact and contact forces.

Experiments of the rolling mode showed similar results to simulations, in terms of rolling/sliding phases and the contact force dependency of the mode switch. Note that it is very difficult to make a quantitative comparison between experimental and simulated results, as adhesion and friction parameters are not well-known and they depend highly on the environment. Moreover, the force sensing of the AFM probe measures is only on its perpendicular axis: only $F_{\mathrm{ot}}^{\mathrm{N}}$ is measured, not $F_{\mathrm{ot}}^{\mathrm{T}}$. Also, the orientation error θ cannot be obtained exactly and the manipulated objects are rarely perfect spheres. Nevertheless, the general behavior of the system is satisfactory

and proves that implemented force and vision controls allow controlled rolling and sliding, with real-time deduction of object position relative to the gripper.

The improvement of sensing capabilities of the system will enhance the quality and precision of the pick-and-place operation. An AFM probe with bi-directional force sensing would permit controlled rolling in transverse direction. In this way, both $F_{\mathrm{ot}}^{\mathrm{N}}$ and $F_{\mathrm{ot}}^{\mathrm{T}}$ can be accurately measured. Moreover, as the rolling distance would be considerably shorter, one can expect a lower sensibility of the final positioning error on the rolling conditions. The inclusion of the system in a controlled environment would also allow its use for mechanical characterisations, as described in Section 3.3 or for further study of the influence of environmental parameters on adhesion phenomena and friction.

Also, enhanced user interaction is to be provided through an haptic force–feedback interface. This set-up allows to accomplish of complex manipulation tasks as all the advanced robotics aspects of the system become transparent to the user.

REFERENCES

1. A. Menciassi, A. Eisenberg, I. Izzo and P. Dario, From 'macro' to 'micro' manipulation: Models and experiments, *IEEE/ASME Transactions on Mechatronics* **9**, 311–320 (2004).
2. F. Aral and T. Fukuda, Adhesion forces reduction for micromanipulation based on micro physics, in: *Proc. IEEE MEMS*, pp. 354–359 (1996).
3. R. Fearing, Survey of sticking effects for micro parts handling, in: *Proc. IEEE/RSJ Intelligent Robots Syst.*, pp. 212–217 (1995).
4. S. Saito, H. Miyazaki and T. Sato, Micro-object pick and place operation under sem based on micro-physics, *Journal of Robotics and Mechatronics* **14**, 227–237 (2002).
5. F. Aral, A. Kawaji, P. Luangjarmekorn, T. Fukuda and K. Itoigawa, Three-dimensional bio-micromanipulation under the microscope, in: *Proc. of the International Conf. on Robotics and Automation, Vol. 1 (ICRA 2001)*, pp. 604–609 (2001).
6. Y. Rollot, S. Haliyo, S. Régnier, L. Buchaillot, J. Guinot and P. Bidaud, Experimentation on micromanipulation using adhesion forces in unconstrained environment, in: *Proc. of the IEEE/RSJ International Conference on Intelligent Robots and Systems (IROS 2000)*, Japan, pp. 653–658 (2000).
7. S. Haliyo, Y. Rollot and S. Régnier, Manipulation of micro-objects using adhesion forces and dynamical effects, in: *Proceedings of ICRA/IEEE International Conference on Robotics and Automation* (2002).
8. S. Haliyo, S. Régnier and J.-C. Guinot, [mü]mad, the adhesion based dynamic micro-manipulator, *European Journal of Mechanics A/Solids* **22**, 903–916 (2003).
9. J. Israelachvili, *Intermolecular and Surface Forces.* Academic Press, San Diego, CA (1991).
10. Y. Rollot, S. Regnier and J.-C. Guinot, Dynamical model for the micromanipulation by adhesion: Experimental validations for determined conditions, *Journal of MicroMechatronics* **1**, 273–297 (2002).
11. K. Johnson, *Contact Mechanics.* Cambridge University Press, Cambridge (1985).
12. B. V. Derjaguin, V. Muller and Y. P. Toporov, Effect of contact deformations on the adhesion of particles, *Journal of Colloid and Interface Science* **53**, 314–326 (1975).
13. S. Saito, M. H., S. T. and T. K., Kinematics of mechanical and adhesional micromanipulation under a scanning electron microscope, *Journal of Applied Physics* **92**, 5140–5149 (2002).
14. D. Maugis, Adhesion of spheres: the j.k.r-d.m.t transition using a dugdale model, *Journal of Colloid and Interface Science* **150**, 243–269 (1992).

15. M. Sitti and H. Hashimoto, Teleoperated touch feedback of surfaces at the nanoscale: Modeling and experiments, *IEEE/ASME Trans. on Mechatronics* **8**, 287–298 (2003).
16. B. Bhushan (Ed.), *Tribology Issues and Opportunities in MEMS.* Kluwer Academic Publishers, Dordrecht (1998).
17. L.-O. Heim, J. Blum, M. Press and B. Hans-Jrgen, Adhesion and friction forces between spherical micrometer-sized particles, *Physical Review Letters* **83**, 3328–3331 (1999).
18. N. Brilliantov and T. Pschel, Rolling as a continuing collision, *The European Physical Journal B* **12**, 299–301 (1999).
19. D. S. Rimai and D. J. Quesnel, *Fundamentals of Particle Adhesion, Polymer Surfaces and Interfaces*, M. W. Urban (Ed.). Global Press (2001).
20. S. Saito, H. Miyazaki, T. Sato, K. Takahashi and T. Onzawa, Dynamics of micro-object operation considering the adhesive effect under an sem, in: *Proc. of Photonics Intelligent Systems and Advanced Manufacturing, Microrobotics and Microassembly*, pp. 12–23. SPIE (2001).

ABOUT THE AUTHORS

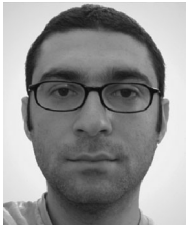

D. Sinan Haliyo was born in Istanbul in 1976. He obtained his PhD in 2002, in Robotics, at Université Pierre et Marie Curie (Paris, France). Currently, he is Associate Professor at Laboratoire de Robotique de Paris and works mainly on micro- and nano-manipulation and related topics, such as remote handling and micro-scale phenomena.

Fabien Dionnet was born in France on December 29, 1977. He received in 2001 the Engineer Diploma from the ENSPS, National School of Higher Education of Physics of Strasbourg (Strasbourg, France), and the MS degree in Photonics, Computer Vision and Cybernetics from the Louis Pasteur University (Strasbourg, France). He recently received the PhD degree in Mechanics and Robotics from the University Pierre et Marie Curie. His research interests are focused on visual servoing, force-feedback control and haptics for robotic and microrobotic systems.

Stéphane Regnier received his PhD degree in Mechanics and Robotics from the University Pierre et Marie Curie (Paris, France) in 1996. Currently, he is Associate Professor at the Laboratory of Robotics of Paris. From 2001 to the present day, he has been head of the micromanipulation team of the Laboratory of Robotics of Paris. His research interests are focused to micro-scale phenomenona, such as micromechatronics and biological cell micromanipulation.